INORGANIC CHEMISTRY
FRONTIERS

RESEARCH ARTICLE

View Article Online
View Journal | View Issue

Cite this: *Inorg. Chem. Front.*, 2024, **11**, 286

Mechanistic studies on the formation of ternary oxides by thermal oxidation of the cubic laves phase $CaAl_2$†

Elias C. J. Gießelmann, [a] Stefan Engel, [a] Johannes G. Volpini, [b] Hubert Huppertz, [b] Guido Kickelbick *[c] and Oliver Janka *[d]

Oxide materials are of key importance in many aspects of everyday life. However, their solid-state syntheses require high temperatures and often multiple steps when conducted from the binary oxides. Herein, we report a proof-of-concept investigation addressing the possibility to synthesize oxides from a phase-pure, well-defined, and highly crystalline intermetallic starting material *via* oxidation with elemental oxygen. The thermal oxidation behavior of the cubic Laves phase $CaAl_2$ was investigated under various atmospheric environments by thermal analysis or by different bulk synthesis techniques. Besides different furnace types, also varying O_2 concentrations and different heating rates, and annealing times were explored. Interestingly, the reaction progresses *via* the intermediate $Ca_{12}Al_{14}O_{33}$ (12 CaO·7 Al_2O_3) before the expected stoichiometric oxidation product, monoclinic $CaAl_2O_4$ (CaO·Al_2O_3), is finally observed. This is highly surprising, since the intermediate has a different Ca to Al ratio compared to the starting material. Different strategies were employed to optimize the synthetic conditions and to decipher the reaction mechanism. The formation of the various products was followed by a detailed analysis of the powder X-ray diffraction data *via* Rietveld refinements and additionally by ^{27}Al MAS NMR experiments, while quantum-chemical calculations supported the proposed reaction mechanism.

Received 16th August 2023,
Accepted 11th November 2023

DOI: 10.1039/d3qi01604h

rsc.li/frontiers-inorganic

1 Introduction

Lightweight alloys, based on Mg, Al, Ti, or Be are an important class of materials for a plethora of modern technical applications ranging from automotive and transportation applications[1–4] to architecture,[5,6] to corrosion resistant parts for air- and spacecrafts,[7–11] non-sparking tools,[12,13] all the way to materials for medical applications like stents or implants.[9–11,14] Intermetallic compounds play an important role in some of these alloys. For example, the most commonly used aluminum-based alloys (Al–Cu or Al–Mg–Cu) get their significantly improved mechanical properties, with respect to elemental Al, from the formation of intermetallic precipitations like $CuAl_2$ ($I4/mcm$ [15]) or $MgCuAl_2$ (S-phase, $Cmcm$ [16]).[1,17–19]

The chemical and thermal resistance as well as the mechanical properties of some of these materials are astonishing.[20] Alloys from the Ti–Al system for example are described as some of the best materials for aircraft and gas turbines due to their low density and high mechanical strength.[21,22] However, their corrosion resistance, especially at high temperatures, is insufficient, thus, alloying with different elements or defined structuring was employed.[23–25] Therefore, oxidation studies of these compounds are an important field of research.[25–29] Ni–Al alloys, in contrast, are of great importance when it comes to corrosion stability under extreme conditions. It has been shown in NiAl, that aluminum atoms, due to their high oxophilicity, form a protective layer of aluminum oxide Al_2O_3 (corundum, space group $R\bar{3}m$) when exposed to air at elevated temperatures, protecting the unreacted substance underneath.[30–32] The addition of small amounts of $CaAl_2$ to an aluminum alloy was shown to increase the protection of the surface from damage through oxidation.[33]

From a synthetic and preparative point of view, the oxidation of intermetallics or alloys could be used to synthesize ternary oxides from binary starting materials, quaternary oxides from ternary phases and so on. Hoppe and co-workers prepared different AMO_2 phases (A = Li–K, M = In, Tl) from the Zintl phases NaTl, KTl, and LiIn.[34–36] Also, CsAuO could be obtained by the reaction of CsAu with dry O_2.[37] The high-temp-

[a]*Inorganic Solid-State Chemistry, Saarland University, Campus C4.1, 66123 Saarbrücken, Germany*
[b]*Institute for General, Inorganic and Theoretical Chemistry, University of Innsbruck, Innrain 80-82, 6020 Innsbruck, Austria*
[c]*Inorganic Solid-State Chemistry, Saarland University, Campus C4.1, 66123 Saarbrücken, Germany. E-mail: guido.kickelbick@uni-saarland.de*
[d]*Inorganic Solid-State Chemistry, Saarland University, Campus C4.1, 66123 Saarbrücken, Germany. E-mail: oliver.janka@uni-saarland.de*
† Electronic supplementary information (ESI) available. See DOI: https://doi.org/10.1039/d3qi01604h

erature superconductor $YBa_2Cu_3O_{7-\delta}$ [38] could also be prepared by the oxidation of BaCu and YCu as well as related compounds.[39–41] Jung and coworkers finally used a wide variety of homo- and heterogeneous alloys for the synthesis of a plethora of different oxides.[42–50] For example, Tl/Ni/P alloys were used for the synthesis of different phosphates, *e.g.* $TlNi_4(PO_4)_3$, $Tl_4Ni_7(PO_4)_6$, and $Tl_2Ni_4(P_2O_7)(PO_4)_2$ [42] while the oxide-oxovanadate $TlCu_5O(VO_4)_3$ [50] was obtained from Tl/Cu/V alloys.

However, studies that closely examine the specific oxidation behavior of a phase-pure and well-defined intermetallic compound as a starting material are rare. One example is from Grin and coworkers reporting on the behavior of $CaAg_2$ in catalytic ethylene epoxidation reactions.[51] They observe the formation of elemental Ag besides Ca_2Ag_7 and CaO, $Ca(OH)_2$ as well as $CaCO_3$ based on the different reaction pathways during catalysis. Furthermore, due to the large variety with respect to composition and elemental combinations, one could think about using binary intermetallics as starting materials for the synthesis of *e.g.*, new ternary oxides/chalcogenides/halides that might not be targetable *via* classic reactions of the respective binary oxides/chalcogenides/halides. Moreover, one can learn a lot not only about the stability of the intermetallic compounds, but also about the formation of the reaction products and the underlying reaction mechanisms. One of the rare studies applying this approach was successfully presented by Hoch and coworkers synthesizing ternary compounds in the system $Li_xGa_yX_z$ (starting with the equiatomic LiGa intermetallic and X = N, S, O).[52]

The present paper focuses on the oxidation of the cubic Laves phase $CaAl_2$ ($Fd\bar{3}m$). One might immediately think of $CaAl_2O_4$ ($CaO{\cdot}Al_2O_3$; CA; $P2_1/c$)[53] as the most likely oxidation product since it has the same Ca to Al ratio as the intermetallic compound. In addition to the RT phase, two high-pressure polymorphs (own type, $P2_1/m$; $CaGa_2O_4$ type, $P2_1/c$, CaV_2O_4 type, *Pnma*) have been reported.[54,55] Other oxides in the ternary system Ca–Al–O, that might be possible oxidation products, are *e.g.* orthorhombic $Ca_5Al_6O_{14}$ (5 $CaO{\cdot}3\ Al_2O_3$; C5A3; $Cmc2_1$),[56] cubic $Ca_3Al_2O_6$ ($3CaO{\cdot}Al_2O_3$; C3A; $Pa\bar{3}$)[57] or cubic $Ca_{12}Al_{14}O_{33}$ (12 $CaO{\cdot}7\ Al_2O_3$; mineral mayenite, C12A7; $I\bar{4}3d$).[58] The latter one has gained a lot of attention within the last two decades due to its ability to form an electride.[59–61] In the course of this paper, different approaches to oxidize $CaAl_2$ are described along with thermoanalytical investigations, compositional studies *via* Rietveld refinements of the powder X-ray diffraction data, ^{27}Al NMR studies, and DFT calculations to investigate the respective stabilities leading to a concise picture of the oxidation mechanism of $CaAl_2$.

2 Experimental

2.1 Synthesis

Precursor $CaAl_2$. Calcium pieces (ChemPur, Karlsruhe, Germany, 99.5%) and aluminum pellets (Onyxmet, Olsztyn, Poland, 99.99%) were used as received as starting materials for the synthesis of the intermetallic precursors $CaAl_2$ and nominal "Ca_6Al_7". The binary starting materials were prepared on a 350 mg (nominal Ca_6Al_7) and 400 mg ($CaAl_2$) scale. The Ca pieces were stored under an argon atmosphere, surface contaminations were removed mechanically prior to use. The synthesis of the binary compounds was carried out in a custom-build arc furnace. Elements were transferred under argon into a water-cooled copper hearth and arc melted under dried argon at 800 mbar.[62] The argon was purified prior to use with titanium sponge (873 K), silica gel, and molecular sieves. To avoid evaporation of Ca, the Al pieces were piled on top and enclosed in Al foil. Careful melting created an encapsulation of the Ca pieces. The resulting bead was turned over and remelted three times to increase the homogeneity. The weight loss in all cases was <1 mass%. As-cast samples are silver metallic, ground powders are grey and stable in air over months.

Solid-state synthesis. The conventional solid-state synthesis was carried out in a chamber furnace (HTC 03/16/P330, Nabertherm, Lilienthal Bremen, Germany) under ambient conditions starting from of $Ca(NO_3)_2{\cdot}4\ H_2O$ (Merck, Darmstadt, Germany, ≥99.0%) and $Al(NO_3)_3{\cdot}9\ H_2O$ (Merck, Darmstadt, Germany, ≥99.99%) with molar ratios of 1 : 1 and 1 : 2. The starting materials were mixed in an agate mortar, transferred to a corundum boat, and heated to 1473 K with a heating rate of 1.6 K min^{-1}. After calcinating for 4 h, the chamber furnace was turned off and the sample was cooled to room temperature.

Oxidation of $CaAl_2$. Oxidation reactions were performed in an STA system (TGA/DSC 1 Star HT/1600 system, Mettler Toledo, Columbus, OH, USA), a muffle oven, a custom-built oxidation tube furnace or in an induction furnace. A muffle oven model N 11/Hr (Nabertherm, Lilienthal Bremen, Germany) with a C30 temperature control unit was used at ambient pressure and atmosphere. The intermetallic powders were directly used and placed in porcelain (likely to be a mixture of Al_2O_3, SiO_2 and MgO) boats. All oxidation experiments using a muffle oven were performed under air at 1273 K reached within ≈5.5 h (≈3 K min^{-1}). The samples were dwelled at 1273 K for different durations (*vide infra*). Afterwards, the oven was allowed to cool to room temperature with the door closed (≈20 h; ≈1 K min^{-1}).

Oxidation reactions using higher O_2 concentrations were carried out in a custom-built oxidation furnace (Carbolite Gero GmbH & Co. KG, Neuhausen, Germany). The samples were placed in porcelain boats and centered in the tube furnace. The argon was purified prior to use with titanium sponge (873 K). The flow rates of Ar/O_2 or pure O_2 were regulated using variable area flow meters (Kobold Messring GmbH, Hofheim am Taunus, Germany). For the reactions using 50% O_2, the flow rates were 20 mL min^{-1} O_2 and 20 mL min^{-1} Ar, for the reactions using pure O_2 a flow rate of 20 mL min^{-1} was used.

Finally, oxidation reactions were tested in a high-frequency furnace (Typ TIG 5/300, Hüttinger Elektronik, Freiburg,

Germany). For these experiments, the samples were pressed to pellets, placed in corundum crucibles which in turn were placed in the water-cooled reaction chamber and heated to approximately 1073 K under vacuum. After a constant temperature was reached, the sample chamber was opened to air, which exposed the red glowing sample to the atmosphere.

2.2 Thermal analysis

Simultaneous thermogravimetric analysis (TGA) and differential scanning calorimetry (DSC) were carried out with a TGA/DSC 1 Star HT/1600 system (Mettler Toledo, Columbus, OH, USA) under an Ar/O_2 atmosphere with flow rates of 40 mL min^{-1} each. Temperature programs are given with the experiments, the heating rates were typically 20 K min^{-1} if not specified otherwise. Samples were placed into alumina crucibles ($ø$ 6 mm, h = 4.5 mm) for the STA measurements.

2.3 X-ray diffraction

Powder X-ray diffraction (PXRD) patterns of the pulverized samples were recorded at room temperature on a D8-A25-Advance diffractometer (Bruker, Karlsruhe, Germany) in Bragg Brentano θ–θ-geometry (goniometer radius 280 mm) with CuKα-radiation (λ = 154.0596 pm). A 12 μm Ni foil working as Kβ filter and a variable divergence slit were mounted at the primary beam side. A LYNXEYE detector with 192 channels was used at the secondary beam side. Experiments were carried out in a 2θ range of 6–130° with a step size of 0.013° and a total scan time of 1 h. The recorded data was evaluated using the Bruker TOPAS 5.0 software[63] and the fundamental instrument parameters were used to fit the data.

To investigate the phase composition of the powder samples synthesized by the solid-state approach, diffraction experiments were performed on a Stoe Stadi P diffractometer (STOE & Cie. GmbH, Darmstadt, Germany) using Ge(111)-monochromatized primary X-ray radiation ($MoK\alpha_1$, λ = 0.7093 Å) and a Mythen 1K detector (Dectris AG, Baden-Daettwil, Switzerland). Data acquisition and processing were carried out in Winxpow.[64] The X-ray diffraction patterns were taken in the 2θ range from 2.0 to 46.0 with a step size of 0.015° and 29.0 s per step. Rietveld refinements based on the powder data was performed in Topas 4.2.[65]

2.4 Scanning electron microscopy/energy dispersive X-ray spectroscopy (SEM/EDX)

Semiquantitative EDX analyses of the bulk samples were conducted on a JEOL 7000F (Jeol, Freising, Germany) equipped with an EDAX Genesis 2000 EDX detector (EDAX, Unterschleissheim, Germany).

2.5 ^{27}Al solid-state MAS NMR

^{27}Al solid-state MAS NMR spectra were recorded using a Avance III 400 WB (Bruker, Karlsruhe, Germany) at 104.35 MHz using magic-angle spinning (MAS) and static conditions. The samples were used as fine powders. To reduce density and electrical conductivity, samples were mixed with dried sodium chloride in a ratio of 1 : 9 or higher contents of NaCl if the amount of sample was not enough. The diluted samples were loaded into a cylindrical ZrO_2 rotor with a diameter of 4 mm and spun at the magic angle at a frequency of 13 kHz. All experiments conducted were single-pulse experiments with a typical pulse length of 0.83 μs (≈30° pulse) and a relaxation delay of 1 s. Resonance shifts were referenced to an aqueous 1 molar $AlCl_3$ solution. The NMR spectra were recorded using the Bruker Topspin[66] software; the analysis was performed with the help of the Dmfit software.[67]

2.6 Quantum-chemical calculations

Electronic structure calculations of the compounds in the binary and ternary systems Ca–O/Al–O/Ca–Al–O were performed using the projector augmented wave method (PAW) of Blöchl[68,69] coded in the Vienna *ab initio* simulation package (VASP).[70,71] VASP calculations employed the potentials PAW_PBE Ca_sv 06Sep2000, PAW_PBE Al 04Jan2001, and PAW_PBE O_h 06Feb2004. The cutoff energy for the plane wave calculations was set to 800 eV and the Brillouin zone integration was carried out using a k-point mesh with a spacing of ≈0.02 for all compounds.

3 Results and discussion

3.1 Crystal structures and precursor characterization

The cubic Laves phase $CaAl_2$ ($MgCu_2$ type, $Fd\bar{3}m$) was prepared from the elements and characterized by powder X-ray diffraction. Phase pure samples with respect to the measurement technique were obtained and subsequently used in the oxidation experiments. In the cubic crystal structure (a = 804.02(1) pm), the Al atoms (Al on 16c with 0,0,0) form empty Al_4 tetrahedra which are connected over all corners forming a network. The Ca atoms (Ca on 8b with 3/8,3/8,3/8) are found within the cavities of said framework adapting the topology of cubic diamond (Fig. S1†). More information about the structural chemistry of Laves phases can be found in a recent review article.[72] ^{27}Al solid-state NMR investigations showed an intense central line originating from the $|+1/2\rangle \leftrightarrow |-1/2\rangle$ transition which can be modelled with a Gauss-Lorentz fit. The resonance signal can be found at δ = 1091 ppm (Fig. S2†), in line with the literature.[73,74]

$Ca_{12}Al_{14}O_{33}$ (C12A7) sometimes also referred to as $Ca_6Al_7O_{16.5}$, crystallizes in the cubic crystal system with space group $I\bar{4}3d$ (Fig. 1a). The compound can be obtained by solid-state synthesis from the reaction of 12 equivalents of CaO with 7 equivalents of Al_2O_3. However, during single crystal[75] and neutron powder investigations[76] it became clear, that the structure exhibits defects of oxygen atoms (position O3) and the formation of an electride can be observed upon removal of this oxide anion. This is possible by *e.g.* the reaction of the mayenite with Ti or V under an inert gas atmosphere.[60,61] In the crystal structure, the Ca atoms are coordinated by seven oxygen anions (d(Ca–O) = 239–252 pm) in the shape of a dis-

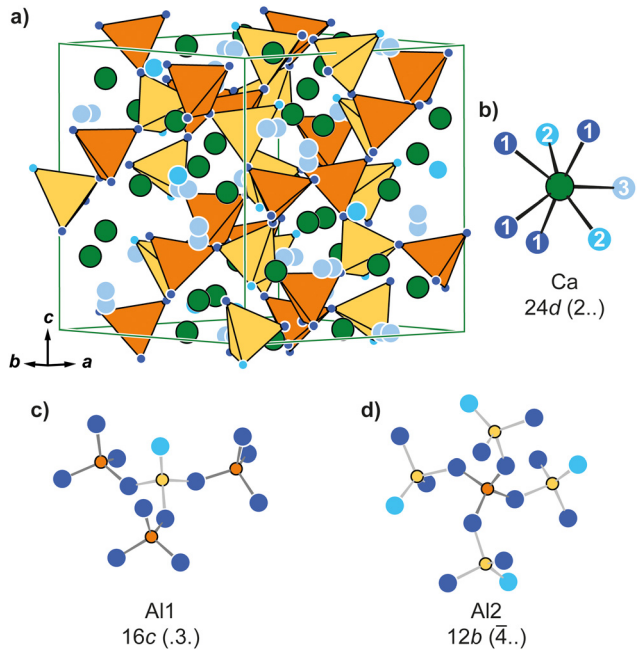

Fig. 1 (a) Unit cell and coordination polyhedron of the (b) Ca atoms in cubic $Ca_{12}Al_{14}O_{33}$ ($I\bar{4}3d$, own type, mayenite). (c) and (d) coordination of the Al1 and Al2 atoms. Ca atoms are depicted in green, Al atoms as light and dark orange, and O atoms as light blue, blue, and cyan circles. The Al1 atoms and their polyhedra are shown in light, the Al2 atoms and their polyhedra in dark orange. The connecting O1 atoms in the [AlO_4] tetrahedra are depicted in blue, the terminal O2 atoms in cyan, and the only partially occupied O3 sites in light blue. Wyckoff positions and site symmetries are given.

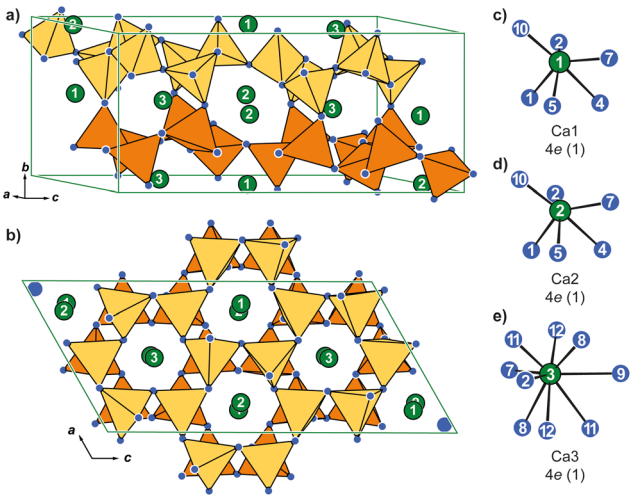

Fig. 2 Unit cell of the of monoclinic $CaAl_2O_4$ ($P2_1/c$, own type) in (a) side view and (b) along [010]. (c–e) Coordination environments of the Ca atoms. Wyckoff positions and site symmetries are given. Ca atoms are depicted in green, Al atoms as orange and O atoms as blue circles. The two layer-like arrangements of the [AlO_4] tetrahedra are depicted in light and dark orange.

torted mono-capped trigonal prism (Fig. 1b), while the two crystallographically distinct Al atoms are tetrahedrally surrounded by four O^{2-} anions and form a network. While all four corners of the [$Al2O_4$] unit (Fig. 1d; d(Al–O) = 172 pm) are connected to [$Al1O_4$] tetrahedra, one corner of the latter is terminal (Fig. 1c; d(Al–O) = 174 + 178 pm). Finally, O3 is not part of the tetrahedral network, but is only found in the coordination environment of the Ca atoms.

$CaAl_2O_4$ crystallizes, despite what one might expect, not in the cubic $MgAl_2O_4$ type (spinel) but in the monoclinic crystal system and adopts its own structure type with space group $P2_1/c$. The [AlO_4] tetrahedra (d(Al–O) = 172–178 pm) arrange as layers in the *ac*-plane formed by six-membered rings with two different topologies (Fig. 2a). In one ring, the [AlO_4] tetrahedra are oriented according to UDUDUD (U = up, D = down) while the neighboring rings orient UUDDUD (Fig. 2b). These layers are stacked along [010] whereas the connected layer has the inverse arrangement of the tetrahedra. Of the three crystallographically independent Ca atoms, Ca1 and Ca2 exhibit significantly deformed octahedral coordination environments (Fig. 2c and d) while Ca3 has nine oxidic neighbors in the shape of a distorted tri-capped trigonal prism (Fig. 2e). The distances in the octahedra (d(Ca–O) = 229–272 pm) are slightly shorter than the ones in the Ca3 polyhedra (d(Ca–O) = 234–317 pm).

3.2 Oxidation of $CaAl_2$ under STA conditions

First reactions targeting the oxidation behavior of the cubic Laves phase $CaAl_2$ were performed in an STA (Simultaneous Thermal Analysis) system. The powdered samples were heated in an Al_2O_3 crucible with two different gas flows of O_2 (reaction gas) : Ar (inert gas) in a 1 : 4 ratio mimicking air as well as in a 1 : 1 ratio for more oxidizing conditions. Fig. 3 and Table 1 summarize the resulting data of the thermal analysis. For all measurements a maximum temperature of 1273 K was chosen, heating rates are given in Table 1. At first, for both gas mixtures, immediate cooling after reaching the maximal temperature was chosen. The mass change remains almost constant until an onset temperature of ≈800 K is reached. An increase of ≈40 mass% can be observed over at least two steps, however, a steady state is reached when reaching the maximum temperature. The heat flow confirms that the oxidation takes place in two close steps due to two signals at $T_{peak,1}$ = 1165 and $T_{peak,2}$ = 1183 K. Using the same experimental conditions in the STA experiments (T_{max} = 1273 K, 20 K min^{-1}) but adding an isothermal section of 5 h at 1273 K leads to a very similar result. The total mass gain is slightly higher (≈50 mass%), however, the onset and peak temperatures in the heat flow are almost identical. Once reaching the maximum temperature, an additional mass gain of ≈8 mass% occurs during the 5 h annealing step. It must be noted that the mass gain is significantly lower compared to the expected mass gain (69 mass%) for the total oxidation of $CaAl_2$ to $CaAl_2O_4$. In both cases, white-grey powders were obtained which are stable in air. The diffraction patterns indicate the formation of mayenite $Ca_{12}Al_{14}O_{33}$ (12 CaO·7 Al_2O_3, C12A7) as the main phase. In addition, the targeted oxidation product $CaAl_2O_4$, as well as elemental aluminum ($Fm\bar{3}m$), and calcium

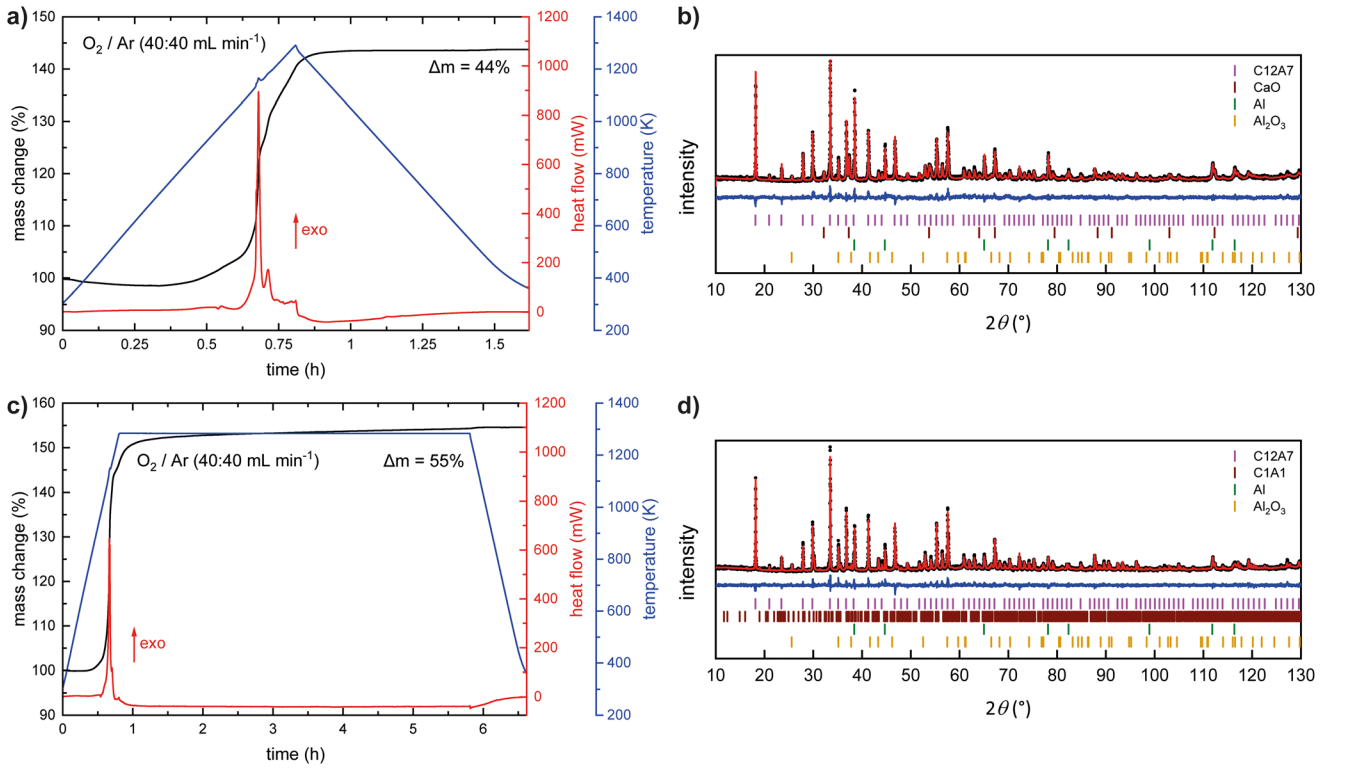

Fig. 3 STA experiments (a and c) and the corresponding Rietveld refinements (b and d) of the collected powder X-ray diffraction data.

Table 1 Results of the Rietveld refinements from powder X-ray diffraction data of the STA treated samples. All specimen were heated to 1273 K with different O_2 : Ar ratios and different dwelling times. The standard deviations for the determined mass% are ±1 mass%

			Phase contributions obtained by PXRD (mass%)						
Ar : O_2 ratio (%)	Dwelling time (h)	Heating rate (K min^{-1})	$Ca_{12}Al_{14}O_{33}$	$CaAl_2O_4$	$Ca_3Al_2O_6$	CaO	Al_2O_3	Al	Figure
80 : 20	0	20	72	7	5	3	3	10	Fig. S3†
	5	20	62	11	10	1	9	7	Fig. S4†
50 : 50	0	5	75	9	1	0	9	6	Fig. S5†
	0	10	73	11	1	0	7	8	Fig. S6†
	0	20	66	8	3	6	6	11	Fig. S7†
	0	40	69	9	5	2	5	10	Fig. S8†
	5	5	71	13	2	0	9	5	Fig. S9†
	5	10	68	14	4	0	9	5	Fig. S10†
	5	20	65	14	2	0	11	8	Fig. S11†
	5	40	56	11	14	2	12	5	Fig. S12†

oxide ($Fm\bar{3}m$) could be identified. Besides a heating rate of 20 K min^{-1}, also heating rates of 5, 10, and 40 K min^{-1} were used, however, the obtained phase compositions are in line with the ones shown before. Table 1 lists the results from the powder X-ray diffraction for the different heating rates and annealing times. The powder X-ray diffraction patterns can be found in the ESI† under the numbers given in the table.

It is interesting to note, that $CaAl_2$ reacts with O_2 and initially forms $Ca_{12}Al_{14}O_{33}$ (mayenite) instead of directly reacting to $CaAl_2O_4$ being the reaction product of a stoichiometric reaction. This is especially surprising since $Ca_{12}Al_{14}O_{33}$ has a different Ca : Al ratio with respect to the starting material $CaAl_2$. However, using prolonged reaction times, $CaAl_2O_4$ is successively formed (Scheme 1). At the same time, the amounts of Al and CaO decrease while more Al_2O_3 is formed. The fact, that $CaAl_2$ vanishes completely but at the same time elemental Al is found gives rise to the hypothesis that the oxidation of the intermetallic phase, which is happening on the surface of the crystalline powder, is accompanied by a decomposition of the Laves phase into CaO and elemental Al, which is subsequently oxidized to Al_2O_3.

What is even more striking is the fact that a 'classical' solid-state reaction starting from $Ca(NO_3)_2{\cdot}4\ H_2O$ and $Al(NO_3)_3{\cdot}9\ H_2O$ shows comparable results. An equimolar reaction of the two salts leads to almost phase pure $Ca_{12}Al_{14}O_{33}$ (Fig. S37†), while a reaction in a ratio of $Ca(NO_3)_2{\cdot}4\ H_2O$ with 2 $Al(NO_3)_3{\cdot}$

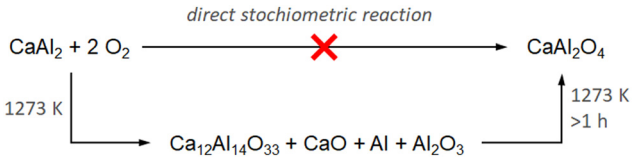

Scheme 1 Reaction pathway for the oxidation of $CaAl_2$ with elemental O_2.

9 H_2O leads to $Ca_{12}Al_{14}O_{33}$, monoclinic $CaAl_4O_7$ (*C*2/*c*), and $CaAl_2O_4$ (Fig. S38†). This is somehow expected, since the reaction occurs from a stoichiometric mixture leading to a Ca-rich besides a Ca-poor phase and the desired reaction product. This clearly shows, that the mayenite type structure is the initial product formed in all these reactions.

To prove that elemental Al is formed during this reaction, ^{27}Al NMR spectra of the oxidation products were recorded. They reveal that the signal of $CaAl_2$ (δ = 1092 ppm) disappears, however, four resonances at δ = 1640, 85, 79, and 11 ppm appear (Fig. 4). The resonance at δ = 1640 ppm corresponds to elemental Al[77–79] while the one at δ = 11 ppm corresponds to Al_2O_3.[80] The rather broad signals at ≈80 ppm can be attributed to $Ca_{12}Al_{14}O_{33}$ according to the literature.[81] Due to the two different coordination environments of the Al atoms (*vide supra*), two signals arise, showing significant overlap. As reported, the sharp signal at $\delta_{iso}(^{27}Al)$ = 79 ppm is caused by the [$Al2O_4$] entities (Q^4) forming the framework while the broad signal at $\delta_{iso}(^{27}Al)$ = 85 ppm originates from the branching [$Al1O_4$] units (Q^3) containing one terminal oxygen atom.

To summarize the STA and solid-state experiments, it can be concluded that all reactions are exothermic, however, instead of $CaAl_2O_4$, the expected oxidation product, first $Ca_{12}Al_{14}O_{33}$ is formed, especially when using short annealing times. In addition, it is quite intriguing, that elemental Al is formed, leading to the assumption, that $CaAl_2$ decomposes into a ternary oxide and elemental Al. Finally, it can be concluded, that the reaction is a surface reaction as the oxidation process stops at a certain point. Therefore, the oxidation in air was performed in different approaches (*vide infra*).

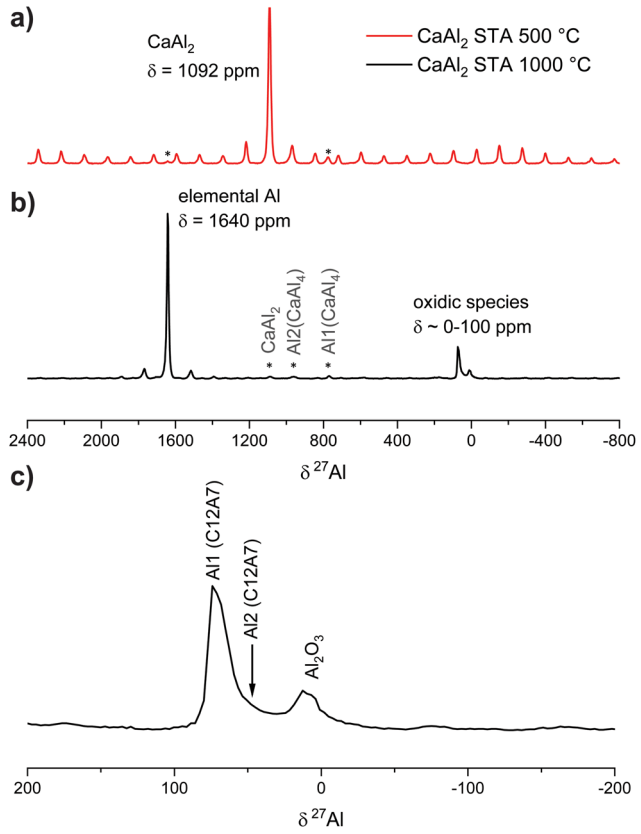

Fig. 4 ^{27}Al NMR investigations of the oxidation product (b) of $CaAl_2$ (a). The full spectrum is shown in the top panels, a zoom of the region of the oxidic species at the bottom (c).

3.3 Oxidation of $CaAl_2$ in air in a muffle furnace

After the observations made during the oxidation reactions carried out in the STA system with different heating rates and O_2/Ar mixtures, bulk oxidations were carried out using air. For these reactions, the powdered $CaAl_2$ sample was treated using different heating schemes (Scheme 2). For all reactions the samples were heated to 1273 K followed by different isothermal steps: (1) annealing of different samples for 1, 5, 48 and 96 h, (2) annealing of the same sample for 1, 1, 5, 10 and 20 h with intermediate grinding of the sample between the heating cycles and (3) 10 cycles of heating a sample to 1273 K followed by direct cooling to RT and subsequent grinding. In addition, five samples were simultaneously heated to 1273 K kept for one hour and analyzed subsequently to get an idea about the standard deviation regarding the chemical composition of the samples. The results of the X-ray diffraction experiments indicate that the product composition is very consistent among this batch of five samples (Table S1†). Fig. 5a–c summarizes

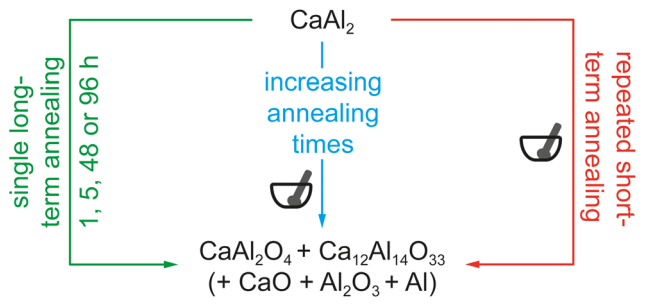

Scheme 2 Illustration of the three different synthetic approaches for the oxidation reaction of $CaAl_2$. For details see manuscript text.

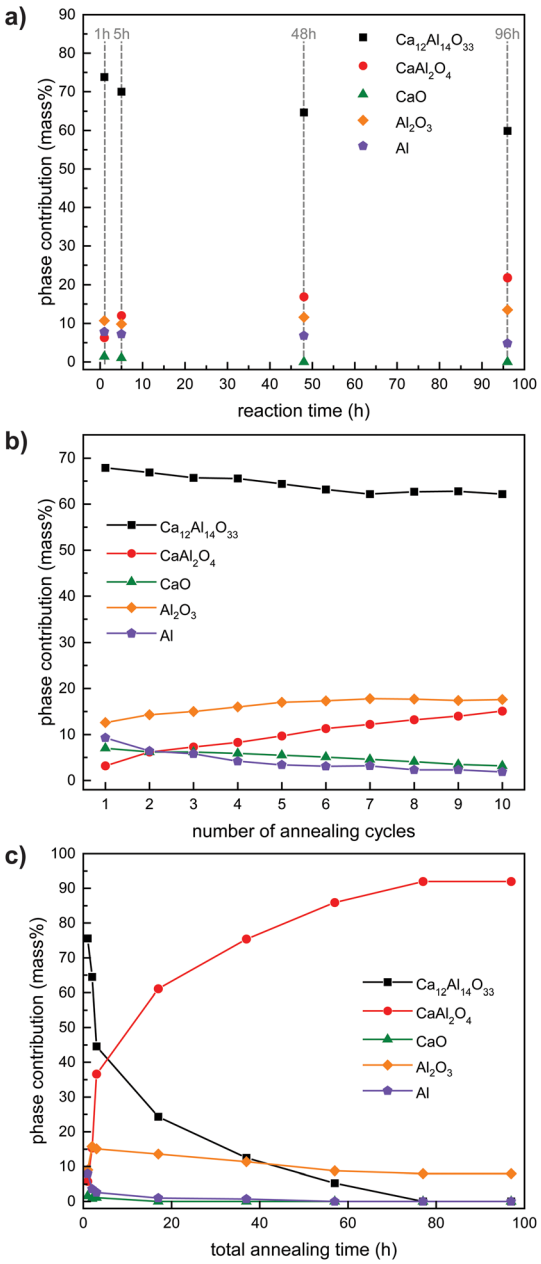

Fig. 5 Results of the Rietveld refinements of the different oxidation approaches of $CaAl_2$. (a) single long-term annealing, (b) repeated heating to 1273 K followed by grinding, and (c) increasing annealing times with intermediate grinding. The values are documented in Table 2.

the results of Rietveld analysis of the products after the muffle oven syntheses (1–3), the numbers are given in Table 2. It is clearly visible, that for all synthesis strategies, $Ca_{12}Al_{14}O_{33}$ is primarily formed. The obtained amount of $CaAl_2O_4$ increases with increasing reaction time in syntheses when only a single oxidation step is conducted (Scheme 2, green; Fig. 5a). However, increasing the reaction time from 1 to 5 to 12 to 24 to 48 to even 96 h only slightly increases the weight-fraction of the targeted oxidation product $CaAl_2O_4$. In the case of multiple short oxidation steps (dwelling only for 1 min at 1273 K) and if the product is ground in blank between (Scheme 2, red; Fig. 5b), the obtained amount of the target phase $CaAl_2O_4$ also increases rather slowly. These observations indicate that long reaction times or multiple steps alone do not lead to the formation of the desired compounds, let alone phase-pure materials. Finally, using a combination of both, prolonged reaction times and multiple annealing steps with in between grinding of the sample, gives the largest amounts of $CaAl_2O_4$ (Scheme 2, blue; Fig. 5c). After five annealing steps with increasing reaction times a maximum of 90 mass% $CaAl_2O_4$ was obtained. In the same fashion, repetitive annealing for 5 h each was conducted over 100 h leading to the same result (Fig. S13 and Table S2†).

The final product described above was also investigated by ^{27}Al NMR spectroscopy. Here, one main signal at δ = 78 ppm is observed (Fig. 6) alongside two minor resonances at δ = 1640 ppm (elemental Al [77–79]) and δ = 14 ppm (Al_2O_3 [80]) and a vast spinning side band manifold originating from the satellite transitions of ^{27}Al (I = 5/2). The chemical shift of the main resonance as well as the quadrupolar interaction (C_Q = 6.5 MHz) and the asymmetry parameter (η = 0.89) is in very good agreement with the literature.[81]

3.4 Oxidation of $CaAl_2$ in different O_2/Ar mixtures

To verify that nitrogen and other atmospheric components do not play a critical role in the described oxidation processes, the reactions were repeated in a tube furnace using a mixture of 50% O_2/50% Ar and 100% O_2 at temperatures of 1273 K and different reaction times. The results from the reactions in the muffle furnaces clearly indicate, that intermediate grinding is key to getting high amounts of $CaAl_2O_4$ in the oxidation product, therefore, the samples oxidized in high O_2 concentrations should give comparable results. Indeed, as documented in Table 3, $Ca_{12}Al_{14}O_{33}$ is formed as the main phase underlining that surface nature of the oxidation, regardless of the O_2 to Ar ratio and the reaction time.

As an intermediate conclusion the following aspects can be summarized:

(1) the oxidation of $CaAl_2$ in O_2/Ar mixtures or in air is a diffusion or even self-limited surface reaction, therefore,

(2) intermediate grinding is essential to remove the oxidic layer and allow for a continuation of the reaction.

(3) Only oxygen seems to play a role in the conducted reactions, N_2 and other constituents of the air are not necessary.

(4) $Ca_{12}Al_{14}O_{33}$ is the initial product in all reactions which subsequently disappears, rendering the mayenite phase the kinetic product while $CaAl_2O_4$ is the thermodynamic product.

Subsequently, two final questions must be addressed: (1) why is $Ca_{12}Al_{14}O_{33}$ formed at first and (2) what is the mechanism of the oxidation?

3.5 Oxidation of $CaAl_2$ in an induction furnace

As already shown, $Ca_{12}Al_{14}O_{33}$ forms as initial (intermediate) product. This compound is significantly richer in Ca compared

Table 2 Summary of the Rietveld fit results of the powder X-ray diffraction data collected from the samples oxidized in a muffle furnace in air. The samples were all heated to 1273 K (≈15 K min^{-1}) with different dwelling times and processing. The standard deviations for the determined mass% are ±1 mass%

		Phase contributions obtained by PXRD (mass%)					
Dwelling time (h)	Total time (h)	$Ca_{12}Al_{14}O_{33}$	$CaAl_2O_4$	CaO	Al_2O_3	Al	Figure
Single long-term annealing							
1	1	73	8	2	10	7	Fig. S14†
5	5	70	12	1	10	7	Fig. S15†
48	48	65	18	0	11	6	Fig. S16†
96	96	60	24	0	11	5	Fig. S17†
Increasing annealing times with intermediate grinding							
1	1	74	7	2	9	8	Fig. S18†
1	2	64	18	1	14	3	Fig. S19†
5	7	44	39	1	14	2	Fig. S20†
10	17	24	62	1	12	1	Fig. S21†
20	37	13	75	0	11	1	Fig. S22†
20	57	6	85	0	9	0	Fig. S23†
20	77	0	92	0	8	0	Fig. S24†
20	97	0	92	0	8	0	Fig. S25†

	Phase contributions obtained by PXRD (mass%)					
Number of cycles	$Ca_{12}Al_{14}O_{33}$	$CaAl_2O_4$	CaO	Al_2O_3	Al	Figure
Repeated heating to 1273 K followed by grinding						
1	72	0	8	11	9	Fig. S26†
2	67	9	6	12	6	Fig. S27†
9	64	16	3	15	2	Fig. S28†
10	63	17	3	15	2	Fig. S29†

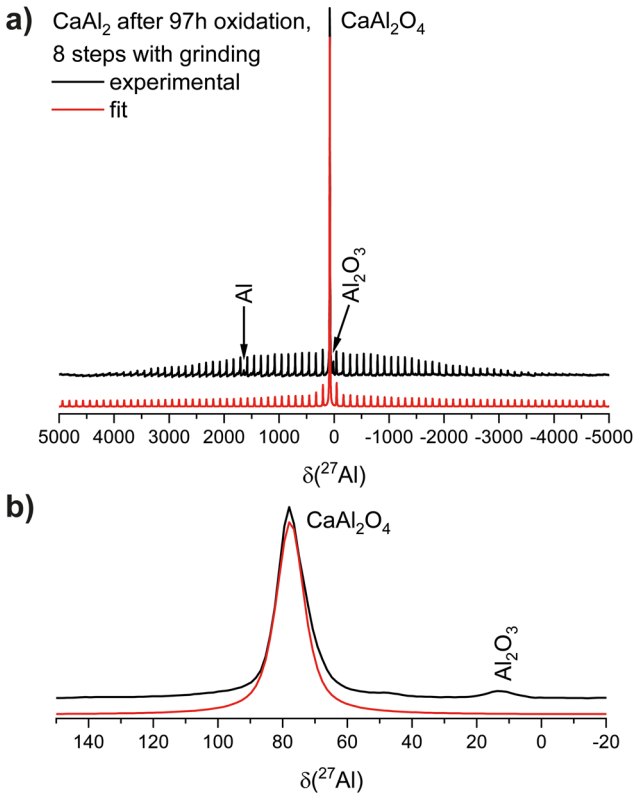

Fig. 6 ^{27}Al NMR investigations of the oxidation product of $CaAl_2$ (black line) plotted *versus* the fitted data (red line). The full spectrum (a) is shown in the top panel, a zoom of the region (b) of the oxidic species at the bottom.

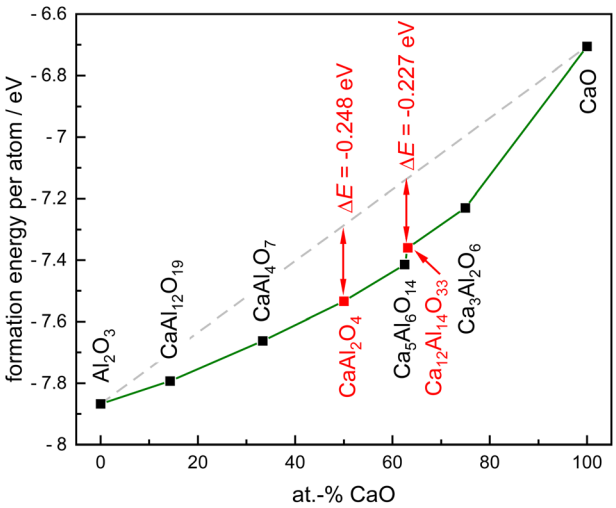

Fig. 7 Convex-hull diagram (formation energy per atom *versus* chemical composition) for the ternary system Ca–Al–O with respect to the binary oxides CaO and Al_2O_3. The formation energy per atom is obtained from DFT calculations.

to the starting material $CaAl_2$. In addition, elemental Al can be observed, leading to two possible scenarios: Ca atoms diffuse to the surface enabling the formation of a more Ca-rich compound or Al atoms diffuse away from the surface leaving a Ca-rich phase. This question has been addressed by the following experiment. A sample of $CaAl_2$ was pressed to a pellet and placed in a corundum crucible inside an induction furnace.

Table 3 Summary of the Rietveld fit results of the powder X-ray diffraction data collected from the samples oxidized in a tube furnace using different Ar to O_2 ratios. The samples were all heated to 1273 K (≈4 K min^{-1}) with different dwelling times

		Phase contributions obtained by PXRD (mass%)						
Ar : O_2 ratio (%)	Dwelling time (h)	$Ca_{12}Al_{14}O_{33}$	$CaAl_2O_4$	$Ca_3Al_2O_6$	CaO	Al_2O_3	Al	Figure
50 : 50	0	73	9	0	0	9	9	Fig. S30†
0 : 100	0	78	3	0	1	9	9	Fig. S31†
0 : 100	5	72	9	2	0	10	7	Fig. S32†

The sample chamber was evacuated and subsequently, the sample was heated to ≈1273 K. At this temperature, the sample chamber was opened to air. Due to the oxidation of the sample, the induction heating is quenched since the formed oxides to not interact with the induction field anymore. The powder X-ray diffraction pattern of the resulting product is shown in Fig. S33†. Besides the expected oxidation product $Ca_{12}Al_{14}O_{33}$ (6 mass%), $CaAl_2$ remains as unreacted educt with 49 mass%. Additionally, CaO (6 mass%) and $CaAl_4$ (39 mass%) can be observed. This unambiguously leads to the conclusion that Ca atoms diffuse to the surface of the particles, leaving the Al-rich intermetallic phase $CaAl_4$. If the Al atoms would be the determining species, elemental Al should have been visible in this experiment.

3.6 Oxidation reactions of the composition 'Ca_6Al_7'

Finally, due to the observation that $CaAl_2$ does not fully oxidize to $CaAl_2O_4$ but forms $Ca_{12}Al_{14}O_{33}$ at first, attempts were made to obtain the latter compound as main product. For this, nominal 'Ca_6Al_7' was prepared by arc-melting of the elements having the Ca : Al ratio equal to that of $Ca_{12}Al_{14}O_{33}$. Characterization by powder X-ray diffraction revealed that a mixture of $CaAl_2$ and Ca_8Al_3 has formed (Fig. S34†). The sample was again investigated *via* STA measurements (heating 20 K min^{-1}, T_{max} = 1273 K, cooling 20 K min^{-1}) with and without an isothermal section of 5 h (Fig. S35 and S36†). In contrast to the previous STA investigations, the TG curves show a two-step mass increase in agreement with the simultaneously measured DSC indicating two exothermic reactions. One signal is observed around $T \approx 823$ K, the second at 1000 K. The latter temperature can be correlated with the oxidation process of $CaAl_2$ described above although the temperature is lowered by almost ≈150 K. The step at lower temperatures therefore must be attributed to the oxidation reaction of the second intermetallic compound present, Ca_8Al_3. Rietveld analysis of the powder diffraction pattern from the oxidation product obtained without the isothermal section revealed the formation of the mayenite phase alongside traces of CaO, Al_2O_3, and elemental Al, similar to the investigations using pure $CaAl_2$ as a precursor. The samples that were dwelled for 5 h at 1273 K showed a decrease of the amount of the mayenite phase in favor of the formation of the Ca-rich cubic oxide $Ca_3Al_2O_6$ ($Pa\bar{3}$)[57] with a significant amount of 21 mass%. This, however, is not that surprising, since Ca_8Al_3 is a Ca-rich compound and therefore most likely the source for cubic $Ca_3Al_2O_6$.

3.7 SEM/EDX

Two samples were additionally investigated *via* EDX. The sample with the highest content of $CaAl_2O_4$, obtained after 97 h of annealing with intermediate grinding (last data point in Fig. 5c and Fig. S25†) as well as the sample obtained by oxidation in pure O_2 after 5 h (Fig. S32†). While the latter contains significant amounts of $Ca_{12}Al_{14}O_{33}$, the first one contains only $CaAl_2O_4$ (≈90 mass%) besides Al_2O_3. Area scans on the sample annealed for 97 h show the expected Ca to Al radio of 1 : 2 (34(1) to 66(1) at%) while the mayenite containing sample exhibits a Ca to Al ratio of 1 : 1.4 (42(1) to 58(1) at%) in good agreement with the 12 : 14 ratio of mayenite.

3.8 Quantum-chemical calculations

To address the final question why $Ca_{12}Al_{14}O_{33}$ is formed as the first oxide, the stability of the different phases in the ternary system Ca–Al–O was investigated *via* quantum-chemical calculations. The formation energy per atom was calculated, resulting in the convex-hull diagram given in Fig. 7. In these plots the stability of the respective oxidic compounds relative to the energy of their constituent binary oxides is shown (Table S3†). At 0 K, every calculated ternary compound can be obtained by the reaction of appropriate amounts of CaO and Al_2O_3 since their formation energy per atom is larger (more negative) than the average energy per atom between the two binaries (dashed line in Fig. 7).

When calculating the energy difference between the formation energy per atom and the average energy per atom, it becomes clear that of the two observed compounds, $CaAl_2O_4$ is the most stable compound (ΔE = −0.248 eV) in this system. However, $Ca_{12}Al_{14}O_{33}$ has only a slightly smaller energy difference (ΔE = −0.227 eV) rendering this compound kinetically stabilized, nicely underlining why this phase is initially formed. In addition, the fact that the $Ca_{12}Al_{14}O_{33}$ can exhibit oxygen vacancies can also play a role here. It could be possible, that the O-deficiencies lead to an entropic stabilization at higher temperatures, however, this cannot be addressed by our calculations.

4 Conclusion

The oxidation of the well-defined, phase-pure, and highly crystalline intermetallic phase $CaAl_2$ ($MgCu_2$ type, cubic Laves phase) was studied by thermal analysis and different bulk oxi-

dation reactions in air and various O_2/Ar mixtures. STA investigations indicate that the oxidation reaction starts above ≈1100 K and is highly exothermic. The observed mass gain (≈40 mass%) is significantly lower compared to an expected full oxidation (69 mass%). Adding a 5 h isothermal section at the maximum temperature of 1273 K leads to a mass gain of about 50 mass%. Powder X-ray diffraction experiments on the oxidation products indicate a multi-phase mixture with cubic mayenite type $Ca_{12}Al_{14}O_{33}$ being the main product. Additionally, Al_2O_3 and elemental Al were observed in significant amounts. The formation of the Al containing compounds, as well as the disappearance of the starting material, was confirmed by ^{27}Al MAS NMR spectroscopy. Bulk studies could show that the oxidation of this intermetallic compound is a surface reaction. However, short reaction times are not sufficient to obtain the expected oxidation product $CaAl_2O_4$. Samples with high amounts of the targeted compound could be obtained by multiple prolonged reactions with intermediate grinding. The formation of the intermediate product $Ca_{12}Al_{14}O_{33}$ was underlined by DFT calculations, which yielded the energy of formation per atom for most known compounds in the ternary Ca–Al–O system. Finally, rapid quenching of the oxidation reaction could prove that the Ca atoms diffuse towards the surface of the particle, explaining the formation of elemental Al as an intermediate. This type of synthesis opens a totally new synthetic approach for ternary and even multinary oxides due to the manifold among the intermetallic starting materials and enables studies on the mechanism of the oxidation of different intermetallics.

Author contributions

Conceptualization by GK and OJ, synthetic work by ECJG, SE and JGV, initial draft of the manuscript by ECJG. ECJG performed the STA and ^{27}Al NMR investigations, SE performed the SEM/EDX investigations, OJ performed the DFT calculations. The entire work was supervised, guided, and revised by GK and OJ. The manuscript was corrected by all authors and finalized by HH, GK, and OJ.

Data availability

Representation of the crystal structure of $CaAl_2$, ^{27}Al NMR spectroscopic data of $CaAl_2$, information on the theoretical calculations, figures and details on the Rietveld refinements can be found in the ESI.†

Conflicts of interest

The authors declare no competing interests.

Acknowledgements

Special thanks goes to Sylvia Beetz from the MWWT/Inorganic Chemistry workshop of Saarland University and to Britta Schreiber from the central glassblowing workshop for installing the furnace for oxidation experiments. Instrumentation and technical assistance for this work were provided by the Service Center X-ray Diffraction, with financial support from Saarland University and German Science Foundation (project number INST 256/349-1) and by the Service Center NMR with financial support from Saarland University and German Research Foundation DFG.

References

1 F. Ostermann, *Anwendungstechnologie Aluminium*, Springer Vieweg, Berlin, Heidelberg, Germany, 2014.
2 C. Kammer, *Aluminium-Taschenbuch 1: Grundlagen und Werkstoffe*, Aluminium-Zentrale, Düsseldorf, Germany, 1995.
3 C. Jaschik, H. Haferkamp and M. Niemeyer, in *Magnesium Alloys and their Applications*, Wiley-VCH Verlag GmbH, Weinheim, Germany, 2000, pp. 41–46, DOI: **10.1002/3527607552.ch7**.
4 M. K. Kulekci, Magnesium and its alloys applications in automotive industry, *Int. J. Adv. Des. Manuf. Technol.*, 2008, **39**, 851–865.
5 Empire State Realty Trust, *Empire State Building Fact Sheet*, **https://www.esbnyc.com/sites/default/files/esb_fact_sheet_4_9_14_14.pdf**.
6 FMGB Guggenheim Bilbao Museoa, **https://www.guggenheim-bilbao.eus/de/**, (accessed 28.06.2023).
7 C. Veiga, J. P. Davim and A. J. R. Loureiro, Properties and applications of titanium alloys: A brief review, *Rev. Adv. Mater. Sci.*, 2012, **32**, 14–34.
8 M. V. Ribeiro, M. R. V. Moreira and J. R. Ferreira, Optimization of titanium alloy (6Al–4 V) machining, *J. Mater. Process. Technol.*, 2003, **143–144**, 458–463.
9 M. Peters, J. Hemptenmacher, J. Kumpfert and C. Leyens, in *Titanium and Titanium Alloys*, Wiley-VCH Verlag GmbH, Weinheim, Germany, 2003, pp. 1–36, DOI: **10.1002/3527602119.ch1**.
10 J. Barksdale, in *The encyclopedia of the chemical elements*, ed. C. A. Hampel, Reinhold Book Corp., New York, USA, 1968, pp. 732–738.
11 P. Enghag, in *Encyclopedia of the Elements: Technical Data – History – Processing – Applications*, ed. P. Enghag, Wiley VCH Verlag GmbH, Weinheim, Germany, 2004, pp. 493–509, DOI: **10.1002/9783527612338.ch18**.
12 E. Gillam, H. P. Rooksby and L. D. Brownlee, Structural relationships in beryllium-titanium alloys, *Acta Crystallogr.*, 1964, **17**, 762–763.
13 O. Janka and R. Pöttgen, The role of beryllium in alloys, Zintl phases and intermetallic compounds, *Z. Naturforsch.*, 2020, **75b**, 421–439.

14 M. Peters and C. Leyens, *Titan und Titanlegierungen*, Wiley-VCH, Weinheim, Germany, 2002.
15 J. B. Friauf, The crystal structures of two intermetallic compounds, *J. Am. Chem. Soc.*, 1927, **49**, 3107–3114.
16 H. Perlitz and A. Westgren, The crystal structure of Al_2CuMg, *Ark. Kemi, Mineral. Geol.*, 1943, **16B**, 1–5.
17 J. R. Davis, *ASM Specialty Handbook: Aluminum and Aluminum Alloys*, ASM International, Materials Park, OH, USA, 1993.
18 O. Janka, in *Applied Inorganic Chemistry*, ed. R. Pöttgen, T. Jüstel and C. Strassert, De Gruyter, Berlin, Germany, 2022, pp. 158–173, DOI: 10.1515/9783110733143-010.
19 D. Altenpohl, *Aluminium und Aluminiumlegierungen*, Springer, Berlin, Heidelberg, Germany, 1965.
20 P. K. Datta, H. L. Du, J. S. Burnell-Gray and R. E. Ricker, in *Corrosion: Materials*, ASM International, Materials Park, OH, USA, 2005, vol. 13B.
21 R. K. Gupta and B. Pant, in *Intermetallic Matrix Composites*, ed. R. Mitra, Woodhead Publishing, Sawston, Cambridge, England, 2018, pp. 71–93, DOI: 10.1016/B978-0-85709-346-2.00004-2.
22 F. Appel, U. Brossmann, U. Christoph, S. Eggert, P. Janschek, U. Lorenz, J. Müllauer, M. Oehring and J. D. H. Paul, Recent progress in the development of gamma titanium aluminide alloys, *Adv. Eng. Mater.*, 2000, **2**, 699–720.
23 C. Kenel, A. Lis, K. Dawson, M. Stiefel, C. Pecnik, J. Barras, A. Colella, C. Hauser, G. J. Tatlock, C. Leinenbach and K. Wegener, Mechanical performance and oxidation resistance of an ODS γ-TiAl alloy processed by spark plasma sintering and laser additive manufacturing, *Intermetallics*, 2017, **91**, 169–180.
24 K. Meng, K. Guo, Q. Yu, D. Miao, C. Yao, Q. Wang and T. Wang, Effect of annealing temperature on the microstructure and corrosion behavior of Ti-6Al-3Nb-2Zr-1Mo alloy in hydrochloric acid solution, *Corros. Sci.*, 2021, **183**, 109320.
25 P. A. Loginov, G. M. Markov, N. V. Shvyndina, G. V. Smirnov and E. A. Levashov, Oxidation resistance of γ-TiAl based alloys modified by C, Si and Y_2O_3 microdopants, *Ceramics*, 2022, **5**, 389–403.
26 S. A. Kekare and P. B. Aswath, Oxidation of TiAl based intermetallics, *J. Mater. Sci.*, 1997, **32**, 2485–2499.
27 Z. Li, W. Gao, Y. He and S. Li, Oxidation of Ti_3Al and TiAl intermetallic compounds under controlled oxygen partial pressures, *High Temp. Mater. Processes*, 2002, **21**, 35–46.
28 R. Pflumm, S. Friedle and M. Schütze, Oxidation protection of γ-TiAl-based alloys – A review, *Intermetallics*, 2015, **56**, 1–14.
29 A. Rahmel, M. Schütze and W. J. Quadakkers, Fundamentals of TiAl oxidation – A critical review, *Mater. Corros.*, 1995, **46**, 271–285.
30 G. Geramifard, C. Gombola, P. Franke and H. J. Seifert, Oxidation behaviour of NiAl intermetallics with embedded Cr and Mo, *Corros. Sci.*, 2020, **177**, 108956.
31 H. J. Grabke, M. W. Brumm and B. Wagemann, The oxidation of NiAl, *Mater. Corros.*, 1996, **47**, 675–677.
32 H. Qin, X. Chen, L. Li, P. W. Sutter and G. Zhou, Oxidation-driven surface dynamics on NiAl(100), *Proc. Natl. Acad. Sci. U. S. A.*, 2015, **112**, E103–E109.
33 Y.-O. Yoon, S.-H. Ha, G.-Y. Yeom, H. K. Lim and S. K. Kim, in *Light Metals 2013*, Springer, Cham, Germany, 2013, pp. 323–326, DOI: 10.1002/9781118663189.ch56.
34 R. Hoppe and H.-J. Röhrborn, Oxidationsprodukte binärer intermetallischer Phasen der Alkalimetalle: $NaTlO_2$ (kubisch) aus NaTl, *Naturwissenschaften*, 1961, **48**, 453–454.
35 R. Hoppe and H.-J. Röhrborn, Oxydationsprodukte intermetallischer Phasen. I. Untersuchungen am $NaTlO_2$, *Z. Anorg. Allg. Chem.*, 1964, **327**, 199–206.
36 R. Hoppe, New routes in the synthesis of metal oxides, II, *J. Solid State Chem.*, 1986, **65**, 127–144.
37 H. D. Wasel-Nielen and R. Hoppe, Oxoaurate(I) der Alkalimetalle: CsAuO, *Z. Anorg. Allg. Chem.*, 1968, **359**, 36–40.
38 P. J. Yvon, R. B. Schwarz, C. B. Pierce, L. Bernardez, A. Conners and R. Meisenheimer, Oxygen isotope effect in $YBa_2Cu_3O_7$ prepared by burning YBa_2Cu_3 in ^{16}O and ^{18}O, *Phys. Rev. B: Condens. Matter Mater. Phys.*, 1989, **39**, 6690–6693.
39 W. Schauerte, H. U. Schuster, N. Knauf and R. Müller, Ein alternativer Weg zur Darstellung von $Bi_2Sr_2CaCu_2O_x$, $YBa_2Cu_3O_{7-\delta}$, und $YBa_2Cu_{3-x}M_xO_{7-\delta}$ (M = Ni, Ag und $x \leq$ 33 Mol%), *Z. Anorg. Allg. Chem.*, 1992, **616**, 186–190.
40 B. Cogel and H. U. Schuster, Oxidationsreaktionen an Legierungen zur Synthese des Hochtemperatur-Supraleiters $Tl_2Ba_2CaCu_2O_8$, *Z. Anorg. Allg. Chem.*, 1993, **619**, 1765–1770.
41 H. Schuster and J. Wittrock, Zur Thermischen Analyse der Oxidation von Abgeschreckten Legierungen als Vorstufen von Hochtemperatursupraleitern, *J. Therm. Anal. Calorim.*, 1993, **39**, 1397–1401.
42 A. Panahandeh and W. Jung, The Oxidation of heterogeneous Tl/Ni/P-alloys - Preparation and crystal structures of the thallium nickel phosphates $TlNi_4(PO_4)_3$, $Tl_4Ni_7(PO_4)_6$, and $Tl_2Ni_4(P_2O_7)(PO_4)_2$, *Z. Anorg. Allg. Chem.*, 2003, **629**, 1651–1660.
43 P. Moser, W. Jung and H. U. Schuster, Die Kristallstruktur von $(Al_{0,5}Ga_{0,5})CuOAsO_4$ – Kupfer zwischen planarer und geschlossener Koordination, *Z. Anorg. Allg. Chem.*, 1997, **623**, 1781–1785.
44 P. Moser and W. Jung, Tl_2CuAsO_4 – ein Zwischenprodukt bei der Oxidation von Tl/Cu/As-Legierungen im Sauerstoffstrom, *Z. Anorg. Allg. Chem.*, 1998, **624**, 1251–1255.
45 P. Moser, H. M. Schwunck and W. Jung, Die Schichtstruktur von $Tl[CuAsO_4]$ und $Tl[CuPO_4]$ mit Zwischenschichten aus Thallium(I) mit stereoaktivem Elektronenpaar, *Z. Anorg. Allg. Chem.*, 1998, **624**, 1256–1261.
46 H. M. Schwunck, P. Moser and W. Jung, Das Kupfer(II)-oxidphosphat $Cu_4O(PO_4)_2$ in einer neuen, orthorhombischen Modifikation durch Oxidation einer Tl/Cu/P-Legierung, *Z. Anorg. Allg. Chem.*, 1998, **624**, 1262–1266.
47 H. M. Schwunck, P. Moser and W. Jung, Das Kupfer(II)-indium-oxidphosphat $CuInOPO_4$ mit α-Fe_2OPO_4-Struktur,

dargestellt durch die Oxidation einer Cu/In/P-Legierung im Sauerstoffstrom, *Z. Anorg. Allg. Chem.*, 1999, **625**, 407–410.

48 H. M. Schwunck, P. Moser and W. Jung, $TlCu^{I}Cu^{II}P_2O_7$ mit Kupfer in gemischter Valenz – ein Zwischenprodukt bei der Oxidation einer Tl/Cu/P-Legierung mit Sauerstoff, *Z. Anorg. Allg. Chem.*, 1999, **625**, 463–466.

49 P. Moser, V. Cirpus and W. Jung, $CuInOVO_4$ – Einkristalle eines Kupfer(II)-indiumoxidvanadats durch Oxidation von Cu/In/V-Legierungen, *Z. Anorg. Allg. Chem.*, 1999, **625**, 714–718.

50 P. Moser and W. Jung, $TlCu_5O(VO_4)_3$ mit $KCu_5O(VO_4)_3$-Struktur - ein Thallium-kupfer(II)-oxidvanadat als Oxidationsprodukt einer Tl/Cu/V-Legierung, *Z. Anorg. Allg. Chem.*, 2000, **626**, 1421–1425.

51 I. Antonyshyn, O. Sichevych, K. Rasim, A. Ormeci, U. Burkhardt, S. Titlbach, S. A. Schunk, M. Armbrüster and Y. Grin, Chemical behaviour of $CaAg_2$ under ethylene epoxidation conditions, *Eur. J. Inorg. Chem.*, 2018, **2018**, 3933–3941.

52 J. Sappl, F. Jung and C. Hoch, Facile one-step syntheses of several complex ionic lithium gallates from LiGa as intermetallic precursors, *Chem. Mater.*, 2020, **32**, 866–873.

53 W. Hörkner and H. Müller-Buschbaum, Zur Kristallstruktur von $CaAl_2O_4$, *J. Inorg. Nucl. Chem.*, 1976, **38**, 983–984.

54 S. Ito, K. Suzuki, M. Inagaki and S. Naka, High-pressure modifications of $CaAl_2O_4$ and $CaGa_2O_4$, *Mater. Res. Bull.*, 1980, **15**, 925–932.

55 B. Lazić, V. Kahlenberg, J. Konzett and R. Kaindl, On the polymorphism of $CaAl_2O_4$ - structural investigations of two high pressure modifications, *Solid State Sci.*, 2006, **8**, 589–597.

56 E. Aruja, The unit cell of orthorhombic pentacalcium trialuminate, $5CaO{\cdot}3Al_2O_3$, *Acta Crystallogr.*, 1957, **10**, 337–339.

57 H. E. Swanson, N. T. Gilfrich and G. M. Ugrinic, Standard X-ray diffraction patterns. Tri-calcium aluminate, $3CaO{\cdot}Al_2O_3$ (cubic), *Natl. Bur. Stand. Circ. (U. S.)*, 1955, **5**, 10–13.

58 W. Büssem, Die Struktur des Pentacalciumtrialuminats, *Z. Kristallogr.*, 1936, **95**, 175–188.

59 S. Matsuishi, Y. Toda, M. Miyakawa, K. Hayashi, T. Kamiya, M. Hirano, I. Tanaka and H. Hosono, High-density electron anions in a nanoporous single crystal: $[Ca_{24}Al_{28}O_{64}]^{4+}(4e^-)$, *Science*, 2003, **301**, 626–629.

60 L. Palacios, Á. G. De La Torre, S. Bruque, J. L. García-Muñoz, S. García-Granda, D. Sheptyakov and M. A. G. Aranda, Crystal xtructures and *in situ* formation study of mayenite electrides, *Inorg. Chem.*, 2007, **46**, 4167–4176.

61 L. Palacios, A. Cabeza, S. Bruque, S. García-Granda and M. A. G. Aranda, Structure and electrons in mayenite electrides, *Inorg. Chem.*, 2008, **47**, 2661–2667.

62 R. Pöttgen, T. Gulden and A. Simon, Miniaturisierte Lichtbogenapperatur für den Laborbedarf, *GIT Labor-Fachz.*, 1999, **43**, 133–136.

63 *Topas, Version 5*, Bruker AXS Inc., 2014.

64 *Winxpow*, STOE & Cie. GmbH, 2015.

65 *Topas, Version 4.2*, Bruker AXS Inc., 2009.

66 *Topspin*, Bruker Corp., 2008.

67 D. Massiot, F. Fayon, M. Capron, I. King, S. Le Calvé, B. Alonso, J.-O. Durand, B. Bujoli, Z. Gan and G. Hoatson, Modelling one- and two-dimensional solid-state NMR spectra, *Magn. Reson. Chem.*, 2002, **40**, 70–76.

68 P. E. Blöchl, Projector augmented-wave method, *Phys. Rev. B: Condens. Matter Mater. Phys.*, 1994, **50**, 17953–17979.

69 G. Kresse and D. Joubert, From ultrasoft pseudopotentials to the projector augmented-wave method, *Phys. Rev. B: Condens. Matter Mater. Phys.*, 1999, **59**, 1758–1775.

70 G. Kresse and J. Furthmüller, Efficient iterative schemes for ab initio total-energy calculations using a plane-wave basis set, *Phys. Rev. B: Condens. Matter Mater. Phys.*, 1996, **54**, 11169–11186.

71 G. Kresse and J. Furthmüller, Efficiency of *ab initio* total energy calculations for metals and semiconductors using a plane-wave basis set, *Comput. Mater. Sci.*, 1996, **6**, 15–50.

72 E. C. J. Gießelmann, R. Pöttgen and O. Janka, Laves phases: superstructures induced by coloring and distortions, *Z. Anorg. Allg. Chem.*, 2023, **649**, e202300109.

73 R. G. Barnes, W. H. Jones and T. P. Graham, Large anisotropic Knight shifts in intermetallic compounds, *Phys. Rev. Lett.*, 1961, **6**, 221–223.

74 S. Engel, E. C. J. Gießelmann, L. E. Schank, G. Heymann, K. Brix, R. Kautenburger, H. P. Beck and O. Janka, Theoretical and ^{27}Al NMR spectroscopic investigations of binary intermetallic alkaline-earth aluminides, *Inorg. Chem.*, 2023, **62**, 4260–4271.

75 H. Bartl and T. Scheller, Zur Struktur des $12CaO{\cdot}7Al_2O_3$, *Neues Jahrb. Mineral., Monatsh.*, 1970, 547–552.

76 A. N. Christensen, Neutron powder diffraction profile refinement studies on $Ca_{11.3}Al_{14}O_{32.3}$ and CaClO $(D_{0.88}H_{0.12})$, *Acta Chem. Scand.*, 1987, **41a**, 110–112.

77 E. R. Andrew, W. S. Hinshaw and R. S. Tiffen, More precise determination of the Knight shift of aluminium, *Phys. Lett. A*, 1973, **46**, 57–58.

78 W.-M. Shyu, T. P. Das and G. D. Gaspari, Direct and core-polarization contributions to the Knight shift in metallic aluminum, *Phys. Rev.*, 1966, **152**, 270–278.

79 C. Benndorf, H. Eckert and O. Janka, Structural characterization of intermetallic compounds by ^{27}Al solid state NMR spectroscopy, *Acc. Chem. Res.*, 2017, **50**, 1459–1467.

80 S. Xu, N. R. Jaegers, W. Hu, J. H. Kwak, X. Bao, J. Sun, Y. Wang and J. Z. Hu, High-field one-dimensional and two-dimensional ^{27}Al magic-angle spinning nuclear magnetic resonance study of θ-, δ-, and γ-Al_2O_3 dominated aluminum oxides: Toward understanding the Al sites in γ-Al_2O_3, *ACS Omega*, 2021, **6**, 4090–4099.

81 D. Müller, W. Gessner, A. Samoson, E. Lippmaa and G. Scheler, Solid-state ^{27}Al NMR studies on polycrystalline aluminates of the system CaO-Al_2O_3, *Polyhedron*, 1986, **5**, 779–785.